Available online at www.sciencedirect.com
SCIENCE DIRECT®
Journal of Nuclear Materials 322 (2003) 204–216
journal of nuclear materials
www.elsevier.com/locate/jnucmat

Room-temperature microindentation behaviour of LWR-fuels, part 1: fuel microhardness

J. Spino *, J. Cobos-Sabate, F. Rousseau

European Commission, Joint Research Centre, Institute for Transuranium Elements, P.O. Box 2340, D-76125 Karlsruhe, Germany

Received 3 April 2003; accepted 16 July 2003

Abstract

Thorough microhardness (H_V) measurements in LWR–UO_2 fuels in the burn-up range 40–100 GWd/t M are described. Two softening processes are found to occur in the fuels during irradiation. The first one appears at the pellet periphery when the local burn-up exceeds ≈70 GWd/t M reflecting mainly the porosity build-up after rim restructuring. The second one affects the whole fuel when it reaches on average ≈70 GWd/t M denoting a bulk irradiation damage release. The rim material is found to acquire the stiffest possible configuration of porous solids showing the lowest property drop as a function of porosity and the largest admissible porosity (≈30%) without undergoing pore-phase opening. By assimilating the hardness data to other property vs. porosity relations, it is predicted that the porous rim material would show a higher Young modulus and thermal conductivity than a low burn-up fuel at equivalent porosity. This ensures not only a stiffer but also a cooler behaviour in reactor.

1. Introduction

The mechanical properties of the pellet material in LWR fuels play an important role in the integral fuel-rod performance, both under steady-state and transient conditions. During power ramps, the probability of the cladding to fail under the pellet expansion depends on the one hand on its ductility at a certain burn-up, and on the other hand on the capability of the fuel to relax interaction stresses via plastic deformation and creep or via microcracking. Also the retention of fission gases in the fuel matrix depends partially on its mechanical behaviour. In this sense, the interconnection of bubbles and pores via crack-paths and therefore the probability of the stored gases to escape to the plenum are conditioned by the propensity (or resistance) of the fuel matrix to undergo local fracture. Besides the normal operation conditions [1], these issues may also become important during abnormal reactor situations, as in the case of the reactivity initiated accidents transients [2], which nowadays is a matter of licensing.

The available mechanical data for irradiated UO_2 is limited and refer only to the low burn-up range (<10 GWd/t M) [3]. Thus, under the present trend aiming at discharge burn-ups ⩾70 GWd/t M [4], studies of the influence of burn-up on the deformation, creep and fracture behaviour of the fuel constitute a real need. Due to the heterogeneous character of the irradiated fuels exhibiting complex crack patterns and rather varied microstructures over the whole radius, the traditional bulk determinations of these properties are inapplicable and might be replaced by local (microgauge) measurements. In this context, the microindentation technique for assessing hardness, fracture toughness and other related properties [5], as well as microacoustic techniques for determining local elastic properties [6] constitute not only appropriate, but cost-efficient alternatives to traditional mechanical tests [7].

In previous publications [8,9], first results of the Vickers hardness (H_V) and the indentation fracture toughness (K_{IC}) of LWR–UO_2 fuels in the range 40–67 GWd/t

* Corresponding author. Tel.: +49-7247 951 233; fax: +49-7247 951 590.
E-mail address: jose.spino@itu.fzk.de (J. Spino).

0022-3115/$ - see front matter © 2003 Elsevier B.V. All rights reserved.
doi:10.1016/S0022-3115(03)00328-3

M were described, showing a hardness decrease and a toughness increase at the pellet periphery. In the present work divided in three parts, these H_V and K_{IC} measurements are respectively extended to the range 80–100 GWd/t M, at the same time their correlations with burn-up, porosity and grain size are elaborated.

In the first part of the work the threshold burn-up for hardness decrease and the hardness vs. porosity dependence are determined. They are in addition correlated with the rim structure onset, the pore structure type and the potential closed–open pore transition of the rim material, this last with impact on fission gas release. Also the hardness vs. porosity dependence is here analysed on the basis of the minimum solid area (MSA) model [10], an alternative interpretation that allows predictions of other 'property vs. porosity relations', as for instance those concerning the variation of the thermal conductivity and the Young's modulus with the pore volume fraction [10].

In the second part of the work the indentation elastic modulus (E) and the E/H_V ratio will be determined. In the third part of the work the indentation crack type and the contributions of porosity and grain size on the fracture toughness (K_{IC}) will be treated, incorporating the previously determined E/H_V ratios in the calculation of the K_{IC} values. Here also the K_{IC} behaviour is discussed in connection with the microcracking propensity of the fuel, which influences the fission gas release and pellet–cladding interaction phenomena. In the last part also similar measurements in MOX-fuels and the fuel–cladding interaction layer are described, helping to visualise the global mechanical behaviour of the fuel at high burn-ups.

2. Experimental

2.1. Fuel characteristics

This first part of the paper deals with UO_2–LWR fuels irradiated in power reactors up to average burn-ups in the range 40–100 GWd/t M and with a test UO_2-fuel rod irradiated in the Belgian BR3-reactor up to 68 GWd/t M, whose post-irradiation characteristics were described elsewhere [11]. In addition, measurements of simulated fuels samples in the range 0–200 GWd/t M, whose preparation and structure properties are described in [12,13], and of a reference non-irradiated UO_2 sample with 3–5% porosity, are included for comparison.

For the standard LWR fuels the initial enrichment was 3.5–4.2 w/o ^{235}U, the initial fuel density 10.40 g/cm^3 and the fabrication grain size of 7–10 μm. The microstructure details and irradiation characteristics of these fuels can be found in Refs. [4,8,13,14]. For the BR3 fuel (68 GWd/t M) much higher enrichment (8.65 w/o ^{235}U) and larger initial UO_2-grain size (≈20 μm) were used [11]. Both these parameter-changes lead to a delayed rim porosity development in the BR3-fuel, comparable to a LWR fuel with only 40 GWd/t M burn-up, and to the lack of grain subdivision in the rim zone [11].

2.2. Sample preparation

Ceramographic cross-sections were carefully prepared in several grinding and polishing steps with hard abrasives up to a surface roughness of about 1 μm, followed by two fine polishing steps with sub-micron oxide suspensions. The last fine surface preparation was aimed at eliminating the residual stresses arising from the grinding step, which otherwise affect the indentation response of the sample, particularly at small loads.

2.3. Microindentation tests

The microindentation tests were performed in hot-cells at room temperature and under protective N_2-atmosphere, using the indentation device of a remote-controlled microscope equipped with a standard Vickers diamond pyramid of 136° edge angle. Tests were performed at a loading and unloading rate of 0.1 N/s, with a hold-time at load of 5 s. The load was determined by an incorporated load cell, with a precision of ±2%. The imprint diagonals and the lengths of the emerging cracks from the indentations corners were measured on the transferred video image of the imprints, with a precision of ±0.5 μm. Determinations were done as a rule 24 h after the tests, allowing strain-relaxation and eventual post-test crack growth to be stabilised. Post-test analysis of the imprint areas was performed by optical microscopy and SEM.

2.4. Measurement conduct

For the standard LWR-fuels the microindentation tests were done at the loads 0.2, 0.5 and 1 N. For each selected load, four orthogonal radii were examined, at radial intervals of 50 μm. Thus, results at constant load included the average of four separate radial profiles, with the error bands placed at the 95% confidence level. The separation between indentations was of the order of 8 imprint diagonals at the load 0.20 N and of the order of 3 imprint diagonals at the load 0.98 N. In this way, even at the highest load applied no overlapping of the individual indentation fields had to be considered. For the BR3-fuel, due to the narrow porous rim-zone available, only tests at 0.20 N load were performed to avoid masking of the microstructure (porosity) gradients when using larger indentation sizes (loads).

2.5. Microhardness (H_V) calculation

Fig. 1 represents schematically a typical Vickers indentation imprint with its deformation and fracture fields, with the vertical cross section showing the

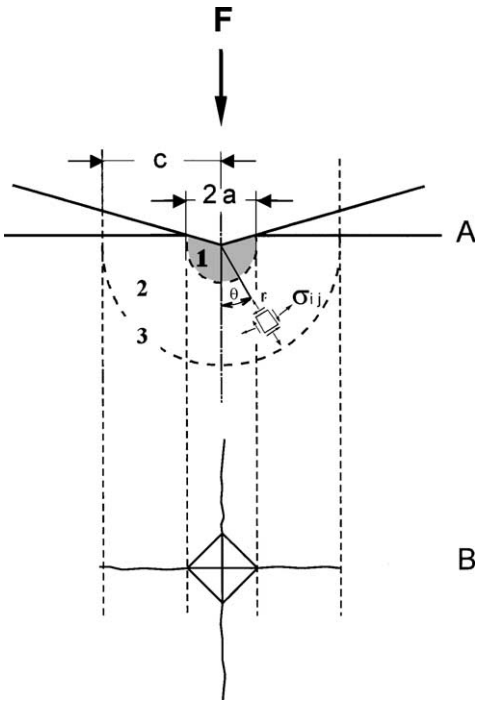

Fig. 1. Vickers indentation cross-section and surface view, with corresponding deformation and fracture fields according to [5]: A. indentation cross-section, B. surface view of square indentation imprint and apex cracks. F = applied load, a = imprint half-diagonal length, b = crack length (accounted from the imprint centre) and σ_{ij} = polar stress-field components. 1 = plastic domain, 2 = elastic domain (also containing the fracture process), 3 = median or half-penny crack boundary underneath the indentation.

characteristic 7:1 ratio between the diagonal length and penetration depth, which results from the particular pyramid apex-angle of 136°. According to this representation, the Vickers hardness of the material is given by the expression

$$H_V = 1.8544 \times 10^{-9} \times F/(2a)^2, \quad (1)$$

where H_V is the hardness given in GPa units, F is the indentation load in N and a is the imprint half-diagonal length in m [15]. As described in Section 3.2.1, due to the variation of the hardness with the indentation load, another sub-index is occasionally added to the H_V designation to indicate the applied load in the test.

3. Results

3.1. Basic indentation behaviour as a function of the pellet radius

The typical indentation response of the irradiated UO_2-fuels examined is summarised in Fig. 2. The figure shows the variation of the print diagonal and crack lengths as a function of the pellet radius for the case of the fuel with 67 GWd/t M burn-up tested at the indentation load 0.5 N. A similar behaviour was observed at other average burn-ups and loads. As usual in the present work, the results indicate the average of four series of measurements at different radii with the scatter band placed at $\pm\sigma$, with σ = standard deviation.

The indentation behaviour appeared typically constant from the fuel centre up to the onset of the rim zone, assumable due to the constancy of the burn-up in the main central part of the fuel (Fig. 2). Within the rim zone, however, continuous imprint enlargement (softening) and crack shortening (toughening) are verified towards the pellet edge, accompanying the microstructure changes in the region. Interesting to remark is that the seemingly toughened zone at the pellet periphery penetrated deeper into the fuel than the observed softened region. Also worthy to mention is that the described shortening of the cracks in the rim region where the porosity increases corresponds to an anomalous case in ceramics. Indeed the common observation indicates decrease of the fracture toughness (K_{IC}) with the increase of porosity, in correspondence with the H_V and E trends [10]. However, although somewhat rare, this behaviour is not without precedents and may be related to local crack branching and bridging [10]. These fracture aspects will be discussed in detail in the third part of the paper dealing with the K_{IC}.

Fig. 3 shows typical indentation imprints at the pellet centre (Fig. 3(a)) and periphery (Fig. 3(b)) of fuels with different average burn-ups. Consistent with the above description, the imprints in the rim region show a clear reduction of the crack diagonal lengths ratio compared to the situation in the fuel centre. As described in Part 2, this causes a marked increase of the fracture toughness (K_{IC}) on approaching the pellet edge.

3.2. Fuel microhardness (H_V) profiles

3.2.1. Influence of the indentation load

Fig. 4 shows the microhardness (H_V) radial profiles of the fuel with 67 GWd/t M average burn-up measured at three different indentation loads. The figure displays also the corresponding porosity profile, as it was obtained by quantitative image analysis [8]. In conjunction with Fig. 2, the results show two well defined zones in the fuel, namely a main inner core with roughly constant hardness and the adjacent rim zone with steadily decreasing hardness towards the pellet edge. As important for the assignation of processes, the boundary between these two zones appears independent of the testing conditions (load). Also interesting to note is the coincidence of the rim-zone widths delimited by the hardness and porosity profiles, whose variations in the rim-region appear roughly inversely proportional (Fig. 4).

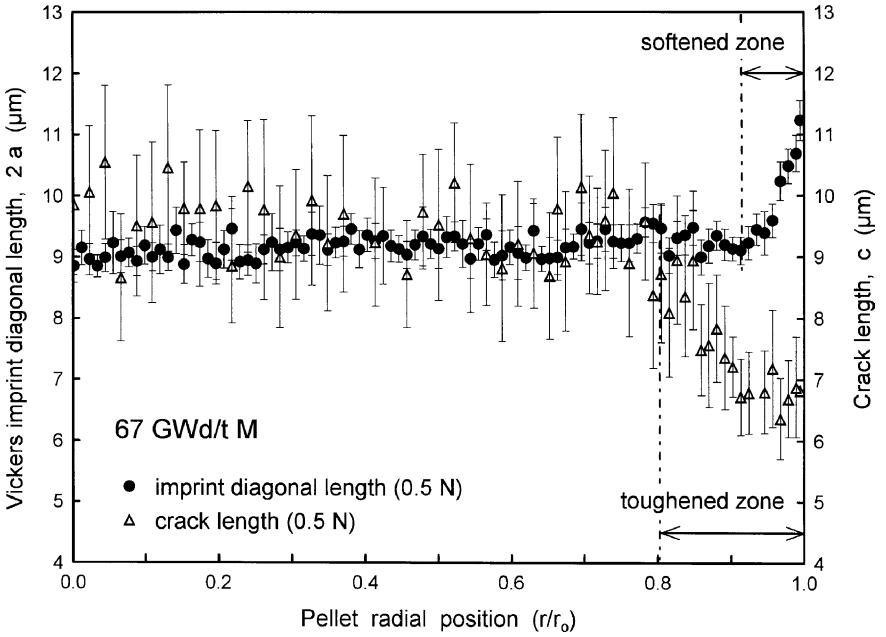

Fig. 2. Typical indentation response of LWR fuels showing the Vickers print diagonal and crack lengths dependence as a function of the pellet radius (study case: LWR fuel 67 GWd/t M, indentation load 0.5 N).

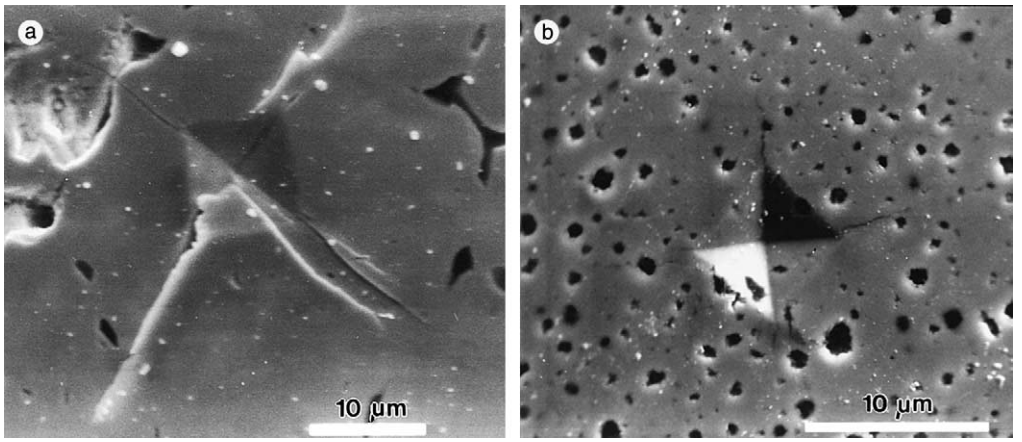

Fig. 3. Representative SEM-micrographs of fuel indentation prints at central and peripheric pellet radial positions: (a) LWR fuel, average burn-up 57 GWd/t M, central fuel position ($r/r_o \approx 0.2$), indentation load 0.49 N, (b) LWR-fuel, average burn-up 67 GWd/t M, rim-zone ($r/r_o \approx 0.98$), indentation load 0.2 N.

With regard to the systematic increase of the hardness on decreasing the indentation load (Fig. 4), this obeys to the so-called 'indentation size effect', which typically affects the indentation tests at low loads [16]. Among various explanations, the most common one assigns this effect to the elastic-retract of the indentation mark after load discharge, which is pronounced at low loads and almost negligible at high loads, e.g. >10 N, where plastic deformation predominates [16]. As a result the hardness values tend asymptotically to a constant level as the indentation load increases [16]. For the comparison of the behaviours at different burn-ups, the load must be therefore kept necessarily as parameter. In our case it was fixed at 0.5 N.

3.2.2. Influence of the average burn-up

Fig. 5 shows the radial variation of the fuel microhardness for three different fuels in the burn-up range 40–80 GWd/t M, as measured at the indentation load 0.5 N. The curves show that the hardness in the central

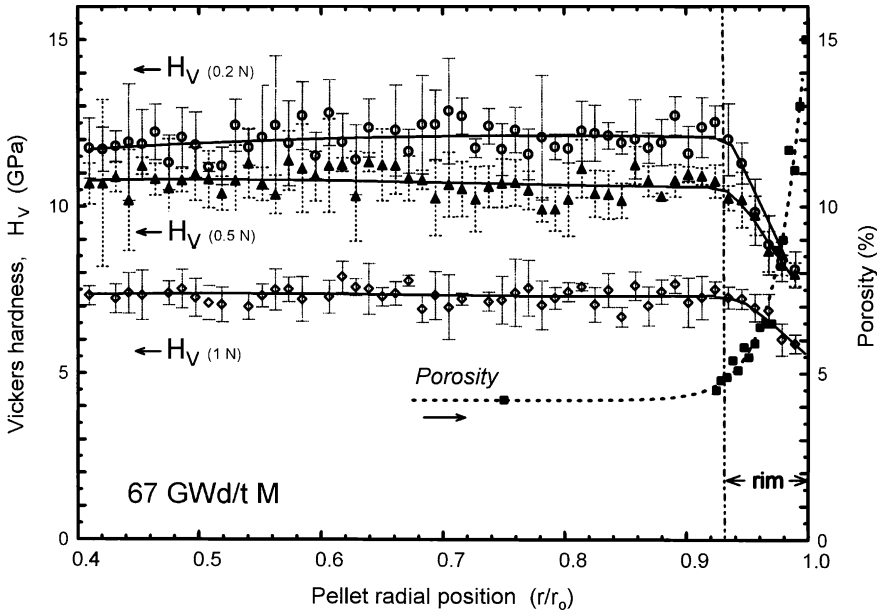

Fig. 4. Variation of the fuel hardness radial profile with the applied indentation load. Comparison with the corresponding porosity profile (study case: LWR fuel 67 GWd/t M).

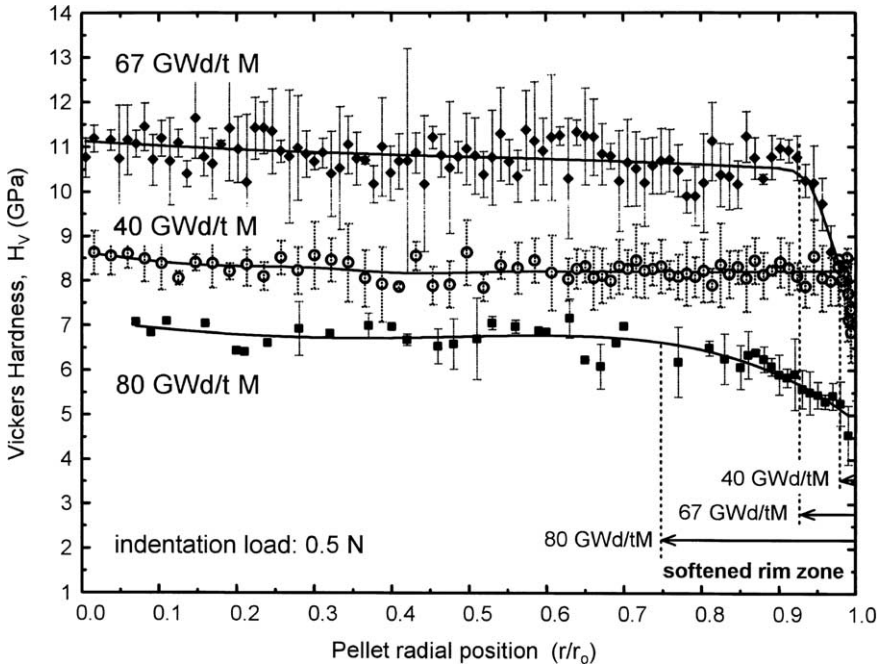

Fig. 5. Variation of the fuel hardness radial profile with the average pellet burn-up (indentation load 0.5 N).

fuel regions increases with burn-up in the range 40–70 GWd/t M and then decreased substantially in the range 70–80 GWd/t M. Furthermore, the localised softening in the rim zone increases its penetration into the fuel with the average burn-up, following approximately the same trend as the corresponding porosity profiles [8,12] (see also Fig. 4).

Thus, while the hardness in the central region appears to be controlled by the average burn-up, the variation at the fuel periphery seems to obey the local

microstructure changes, particularly the porosity growth. Further, due to the moderate irradiation temperatures of the present fuels (<1200 °C [4,14]), the thermal effects on the hardness profiles appear to be negligible. According to Dienst and Brucklacher [17], the room-temperature microhardness of irradiated UO_2 fuels at constant burn-ups should not be modified until the irradiation temperatures reach ≈1400 °C.

Fig. 6 shows the variation of the average hardness in the fuel central regions (i.e. at $r/r_o < 0.8$) with the pellet average burn-up. The values are also compared with the measured data of pure UO_2 and chemically simulated fuels in the burn-up range 0–200 GWd/t M [12,13], all of them obtained at the indentation load (0.5 N). As visible also in Fig. 5, Fig. 6 shows that the total irradiation hardening, which includes both effects of irradiation defects and fission products dissolution–precipitation, increases with burn-up up to ≈70 GWd/t M and then abruptly drops, stabilising at a constant value above ≈90 GWd/t M. On the other hand, the pure chemical hardening increases (though with a lower slope) up to ≈80 GWd/tM and then stagnates, such that at ⩾90 GWd/t M both total and chemical hardenings become almost the same (Fig. 6).

The described drop of the irradiation hardnening at and above 70 GWd/t M indicates an almost complete healing of the accumulated irradiation damage. Apparently, this kind of transformation can occur at any radial position in the fuel, provided that the critical burn-up has been reached and the local irradiation temperatures did not exceed the threshold for thermal defect healing in the reactor (≈1400 °C [17]). Indeed, the threshold around 70–80 GWd/t M in Fig. 6 coincides with the critical local burn-up (≈70 GWd/t M) at which the rim structure has been previously observed at the fuel periphery, as attributed also to defect release and restructuring [13]. This would explain why at somewhat higher average burn-ups (i.e. ∼100 GWd/tM), a recurring rim-like restructuring has been newly observed at intermediate pellet radii, in addition to the usual high burn-up transformation at the fuel periphery [18,19].

4. Correlation of results with key microstructure features

4.1. Influence of porosity

As mentioned in the above section, the variation of the hardness in the rim-zone is likely related to the local microstructure changes. These changes include typically a porosity increase from 2% to 5% (pellet average for $r/r_o < 0.9$) up to 15–17% at the pellet edge, and a grain size reduction of the fuel matrix from originally ≈10 to ⩽0.2 μm [8]. The pellet-edge porosity may even become >20% at burn-ups >80 GWd/t M [18,19]. However, though grain size reduction can contribute to moderate [20] and sometimes considerable hardness increase [21], the main effect on the hardness of the rim zone is expected to arise from the increase of porosity, due to the reduction of the load-bearing area [10].

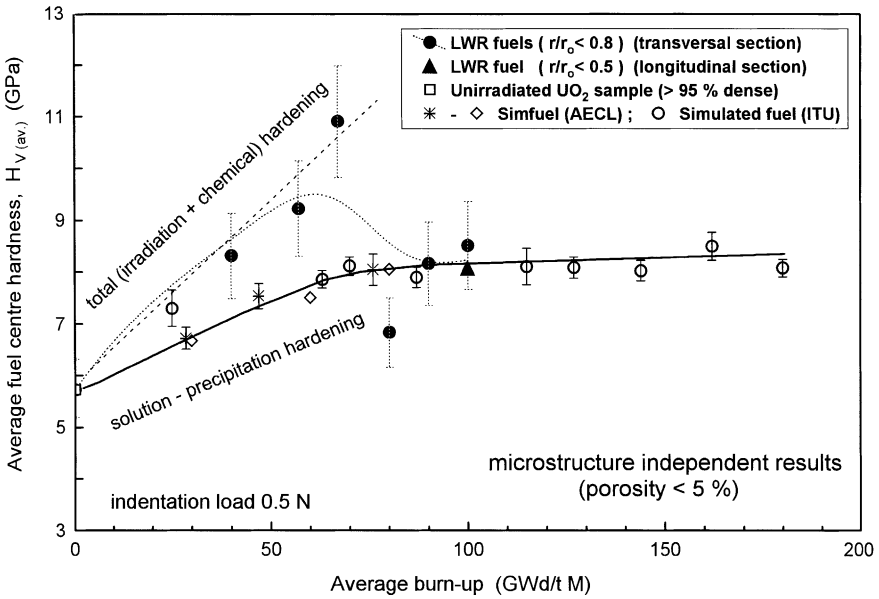

Fig. 6. Average fuel centre hardness ($r/r_o \leqslant 0.8$) as a function of the pellet average burn-up. Comparison with unirradiated and simulated fuel data (indentation load 0.5 N).

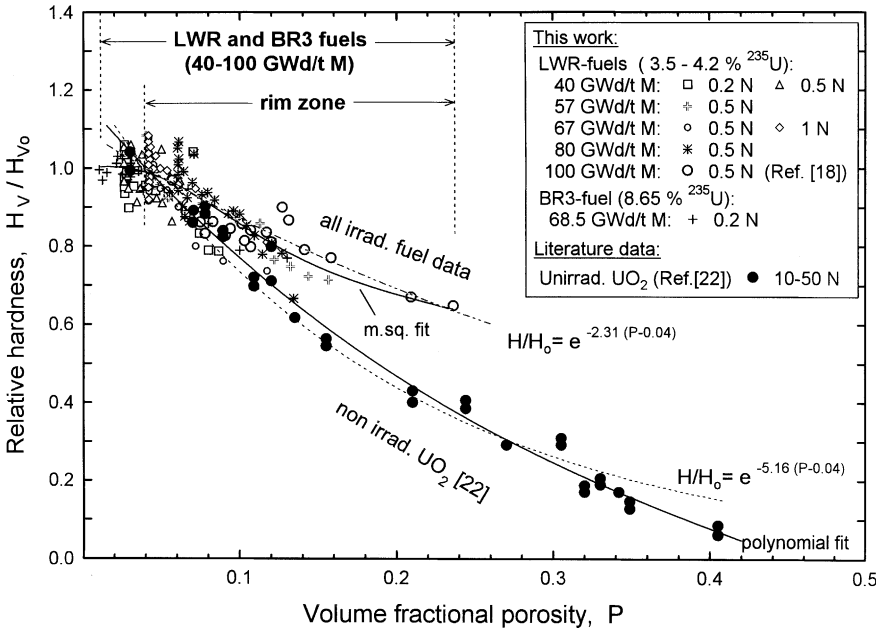

Fig. 7. Relative Vickers hardness vs. fractional porosity data for irradiated LWR fuels (present work) compared to non-irradiated UO_2 data [22]. Reference Vickers hardness values ($H_{V,0}$): (a) *irradiated fuels*: average of data for $r/r_o \leqslant 0.8$ (constant hardness region), same as in Fig. 6, (b) *non-irradiated UO_2*: value at 96% density from Ref. [22] = 5.72 GPa.

To appreciate the above effect, the microhardness results of previous sections were plotted in Fig. 7 as a function of the local porosity for all radial positions in the fuel, using the fractional representation H_V (fuel)/H_V (av., $r/r_o < 0.8$). In this ratio the reference value is the average hardness in the fuel central core, i.e. the zone with approximately constant hardness in Figs. 5 and 6. The local porosity values were taken from previous measurements [8,11,13]. In addition, to confirm the trend at high porosity values, also the data of the 100 GWd/tM fuel described in [19] was added to the plot in Fig. 7.

For comparison reasons, also the literature data for non-irradiated UO_2 in the porosity range 3–40% [22] was added in Fig. 7. In this case also a fractional representation was utilized, taking as reference the hardness of the 96% dense material (= 5.72 GPa, value interpolated from data of Ref. [22]). This reference value was so selected that the curve $H_V/H_{V,0}$ (UO_2) coincided at its value 1 with the onset of the rim zone, i.e. denoting a base (pre-transition) porosity of ≈4% [8,11,13] (Figs. 4 and 7). (Selection of another reference value would cause only a systematic down- or upward shift of the UO_2 data.)

The two sets of $H/H_{V,0}$ data plotted in Fig. 7, therefore intersecting at their value 1 at the fractional porosity 0.04, show different decaying trends with increasing the void fraction, with non-irradiated UO_2 evidencing the larger property deterioration with porosity (Fig. 7). This splitting of the behaviours is a-priori attributed to differences in the corresponding pore types. In Fig. 7 the best fittings for both sets of data are given, namely a polynomial fit for UO_2 and the minimum square fit for the fuel (rim) data. In addition, adjustments with the function $e^{-b \cdot P}$ where b is a constant and P the porosity, with origin at $P_o = 0.04$, are shown in both cases. This exponential function, showing only slightly lower correlation factors than the former best fits (see values in Table 1), correspond to the low P approximation of the 'relative property vs. porosity' curves based on the MSA model [10]. As detailed in next section, the application of this model allows straightforward correlation of the parameter b with the porosity type.

4.2. Role of the pore type

In the above mentioned MSA model by Rice [10,23–27] and other authors [28–30], the basic concept is that the hardness of a porous material, as well as other properties concerning applied stress or flux, is proportional to the MSA fraction (i.e. the load bearing area) perpendicular to the applied load (or flux). According to Ref. [10], the MSA-fraction plots represented logarithmically as a function of P can be divided in three portions, namely an initial lineal part in the low P range (proportional to $e^{-b \cdot P}$ in the normal representation), a transition zone of rapid slope change and a final zone of

Table 1
Fitting parameters of the $H_V/H_{V,0}$ vs. porosity curves in Fig. 7 for irradiated fuels and non-irradiated UO_2

Material	$H_V/H_{V,0} =$	a_1	a_2	a_3	b	R = correlation factor
Unirradiated UO_2	$1+\sum_i a_i \times (P-P_o)^i$	−4.19	6.08	−4.33		0.993
Unirradiated UO_2	$e^{-b\times(P-P_o)}$				5.16	0.987
Irradiated fuel	Minimum square					0.83
Irradiated fuel	$e^{-b\times(P-P_o)}$				2.31	0.75

$H_{V,0}$ (fuel) = average of data at $r/r_o \leqslant 0.8$ (see values in Fig. 6), $H_{V,0}$ (UO_2) = value at 96% density (= 5.72 GPa, interpolated value from data of Ref. [22]), $P_o = 0.04$ = base fuel porosity at rim-onset.

abrupt drop of the MSA (or related property) to zero. This last occurs on achieving the percolation limit of the system (Pc), interpreted as the maximum allowable porosity after which the solid phase disaggregates. At this point the system no longer transmits stress or flux [10].

Accordingly, the data of Fig. 7 are represented in Fig. 8 in semi-log form and compared to the MSA-fraction curves of two ideal systems, i.e. intersecting solid spheres in cubic arrangement and cubic-packed spherical pores in a continuous matrix. As extracted from Refs. [10,23], these curves were plotted with the origin shifted to $P_o = 0.04$, so as to meet at this point the onset of the rim zone as in Fig. 7. The selected cases emulate respectively the fresh (or low burn-up irradiated) and the high burn-up UO_2-fuel materials. Indeed, the system of intersecting solid spheres is commonly used to describe sintered solids, which are characterised by 'pores inherently intergranular and typically smaller than the grains that define them' [10]. On the other hand, the system of immersed pores in a matrix applies more typically to foam-like materials, where 'the ligament walls between pores can reach much smaller dimensions than the characteristic pore size' [10,20,23]. As can be seen in Fig. 9, this last is just the case of the rim-structure at very high burn-ups.

Corroborating the assumptions, the selected MSA-model curves were found to reproduce appropriately the experimental data trends, i.e. in the case of non-irradiated UO_2 up to $P \approx 0.33$ and in the case of the irradiated fuel (rim) for the whole range of measurements ($P \leqslant 0.23$) (Fig. 8). The fitting of the experimental data with a function of the type $e^{-b\cdot P}$ lead to b values of 5.16 and 2.31, respectively for non-irradiated and irradiated UO_2 (Figs. 7 and 8, Table 1). This coincided quite well with the low P-range slopes of the selected analytical MSA-curves, leading respectively to values of $b \approx 5$ for solid spheres and $b \approx 3$ for spherical pores [10].

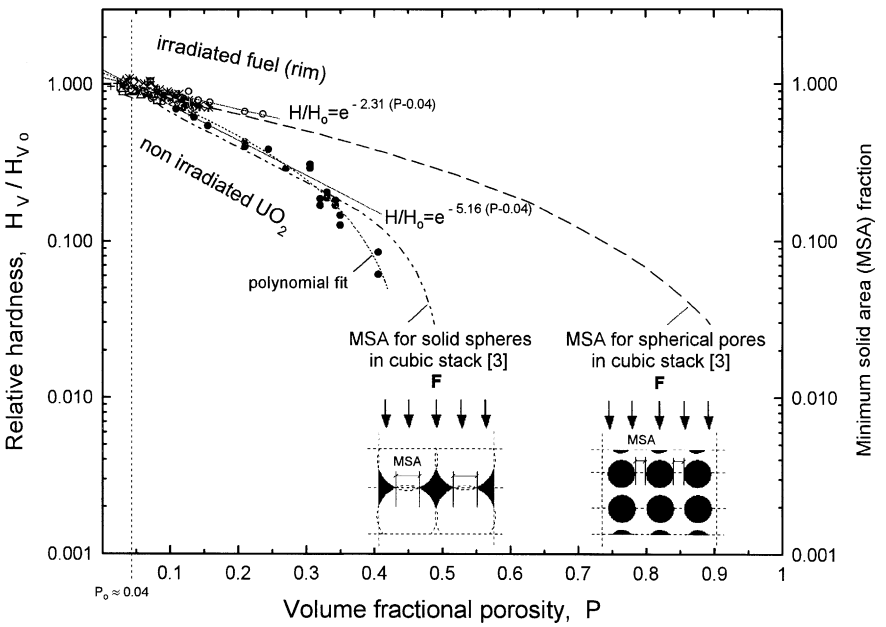

Fig. 8. Same data as in Fig. 7 in log-linear representation as a function of the fractional porosity, compared to MSA-curves for spherical solid particles and pores in cubic packing [10,23–27]. P_o = base fuel porosity at rim onset.

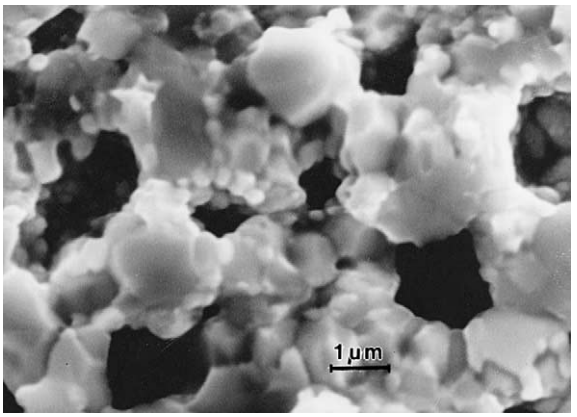

Fig. 9. SEM-micrograph showing details of the rim-structure at very high burn-ups (LWR fuel, average burn-up ≈100 GWd/t M, local burn-up at outermost pellet radial position ≈300 GWd/t M [14]). Note thin, polycrystalline interpore struts (ligaments), eventually thinner than the pore dimension. Average pore size ≈1 μm. Grain size ≈ submicron range. Estimated porosity ≈25%.

4.3. Estimated close–open pore transition in the rim-zone

The MSA-functions derived by Rice [10,26] from topological considerations (e.g., size, shape, coordination number (C_n) of pores and solid particles, etc.) are useful to describe not only the 'property vs. porosity' relations and the percolation limit of the solid phase (P_c), but also the closed–open pore transition of the pore phase (P_{c-o}), i.e. the porosity at which pores become macroscopically interconnected [10]. Although not relevant for the mechanical properties, this transition acquires relevance in flow or permeability applications; in particular for the case of nuclear fuels by signalling the point at which the trapped fission gases could be able to escape to the free volume.

For the interchangeable systems of spherical pores and solid spheres, it was shown that P_{c-o} (spherical pores) $= 1 - P_c$ (solid spheres) and vice versa [10,26]. This was applied to systems with regular distributions of pores and solid particles [10,23–27], whose strict occurrence in practice has been occasionally questioned [31]. However, models considering random distributions of pores and particles led to similar or slightly different P_{c-o} and P_c values [31–33]. In Table 2 some P_{c-o} and P_c results from both geometrical [10,23–27] and random [31–33] models are summarised. It is seen that independently of the kind of pore arrangement, i.e. periodical or random, the porous materials may be characterised by three basic microstructures, i.e. spherical and ellipsoidal pores in a continuous matrix and intersecting solid particles defining cavities, which show in this order decreasing stiffness and decreasing pore connectivity (P_{c-o}) and percolation (P_c) limits (Table 2).

In the case of the rim material, both the micrographs (e.g. Fig. 3(b)) and the H/H_0 vs. P curves (Figs. 7 and 8) suggest that it corresponds to the stiffest possible porous system, i.e. the one represented by spherical pores in a continuous matrix, for which a pore interconnection would occur only at porosity fractions >0.3 (Table 2).

Table 2
Closed–open pore transition and percolation limits (P_{c-o}, P_c) for different microstructure systems according to MSA [10,26] and random models [31–33]

Microstructure system	Coordination number (C_n)		Resultant grain shape	Critical porosity values	
	Particles	Pores		Close–open pore transition P_{c-o}	Solid-phase disruption P_c
Cubic pack of spherical pores [10]		6		0.524	0.964–0.975
Cubic pack of ellipsoidal pores [10]		6		0.524	~1
Cubic pack of solid spheres [10,26]	6	6	Cube	0.035	0.476
Orthorhombic pack of solid spheres [26]	8	5	Hexagonal prism	0.165	0.395
Rhombohedric (fcc,hcp) pack of solid spheres [26]	12	4	Dodecahedron	0.036	0.26–0.32
Body-centered-cubic packing of solid spheres [26]	14	–	Tetrakaidecahedron	0.006	0.06
Random (overlapping) spherical pores (Swiss cheese model) [31,32]		Random		0.3	0.97
Random (overlapping) ellipsoidal pores (aspect ratio 0.25) [31,33]		Random		0.2	0.96 (fitted)
Random overlapping solid spheres [31,32]	Random			0.03	0.7

For interchangeable systems, e.g. spherical pores and spherical particles (either in periodical or random representations) holds P_{c-o} (spherical pores) $= 1 - P_c$ (solid spheres) and vice versa [10,26,31].

This means that at today's burn-up goal for commercial reactors (~70 GWd/t M, peak rim-porosity <17% [8,13]) the porosity of the rim-zone would remain closed, remaining the locally generated fission gases also trapped in the matrix.

In contrast, fuel regions retaining the original (as-sintered) microstructure, e.g. central and intermediate radii regions, may represent the weakest possible porous system configuration, i.e. this defined by intersecting solid particles. This system may exhibit macroscopic pore interconnection already at fractional porosity ≈0.03 (Table 2). From this consideration, occluded fission gases in central fuel regions may be ready to escape under the lightest temperature ramp at any time of the irradiation history, provided $P > 0.03$. This porosity level may be reached e.g. at burn-ups >20 GWd/t M, when the in-reactor densification range has been surpassed [8,14]. Coincidentally, the analysis of released gases in LWR fuels usually show a Xe/Kr ratio corresponding to pellet regions with pre-dominating U fission, i.e. those excluding the rim zone where Pu fission predominates [34].

5. Relation with the pore connectivity from the percolation approach

Similar conclusions as the above are obtained by application of the percolation model developed by Ronchi for MX-fuels [35]. In the cited model an idealised structure of the fuel is proposed with a regular arrangement of pores centred in hypothetical spherical cells larger than the grain size [35], similar to the cubic cells used in [8] to describe the rim structure and to the cells used by Rice [10,27] to describe the system of cubically stacked pores in a matrix.

The pore interlinkage was calculated in [35] by application of the percolation theory, assuming a lattice of sites (pores) connected by randomly distributed bonds (channels or contact points) with certain concentration I = number of bonds/number of sites, with the total site interlinkage occurring when $I = 1.569$, i.e. when each site had available ≈1.6 bonds to share with its neighbours [35,36]. Linked to the structure features, the parameter I, called the interlinkage factor, was assessed by Ronchi [35] as a function of the coordination number of the pore arrangement, the fractional porosity and the grain-to-pore size ratio.

This function I is plotted in Fig. 10 as a function of the grain to pore size ratio s ($s = r_g/r_p$, with r_g and r_p being, respectively, the grain and pore radii), for different porosity fractions and for a simple cubic arrangement of pores ($C_n = 6$). Interesting to remark is that for $s = 5$–7, typical ratios at low burn-ups for 1 μm-pores, the total interlinkage threshold is achieved already in the porosity range 0.01–0.03. On the other hand, for $s = 0.2$–0.3, typical ratios for the rim-zone for 1 μm-pores, the pore interconnection probability remains almost zero (or far below the interlinkage threshold $I \approx 1.6$) up to porosity fractions >0.3 (Fig. 10).

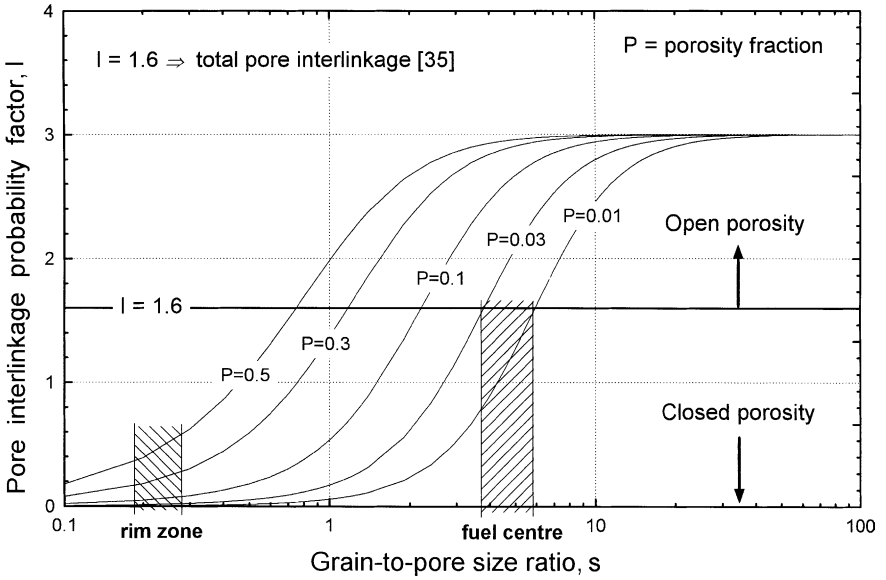

Fig. 10. Pore interlinkage probability factor as a function of the grain to pore size ratio, from Ronchi's site-bond percolation model [35]. $I = 1/2 \times N_p \times \{1 + (1/P - 1) \times (2N_p/\pi) \times [1 - (1 - s^2/(1+s)^2)^{1/2}]/s^3\}^{-1}$ [35]; N_p = pores coordination number, P = fractional porosity; $s = r_g/r_p$ = grain to pore size ratio.

6. Other deduced property vs. porosity relations in the rim zone

Despite the mentioned possible quantitative differences with other model descriptions (Section 4.3), the advantage of the MSA model [10] is that it allows to make predictions of e.g. the thermal behaviour of a porous material, knowing its mechanical response. Key of this is the cited assumption that both mechanical and flux related properties (e.g. thermal or electrical conductivity) are proportional to the load bearing area perpendicular to the applied stress (or flux) [10,20,23–27].

With this in mind, the above results showing a slower decrease of the hardness with porosity in the rim zone of LWR-fuels compared to as-fabricated UO_2 would indicate a similar behaviour for the thermal conductivity of this zone. This situation is illustrated in Fig. 11, where various measured and proposed relative 'property vs. porosity' relations (i.e. Young's modulus (E/E_0) [37], Vickers [22] and Brinell [38] hardness (H/H_0) and thermal conductivity (k/k_0) [39–41]) are shown for the as-sintered and irradiated UO_2 materials.

As for the k/k_0 vs. porosity relation, data may appear wide-spread due to differences in the pore shapes and distributions depending on the fuel history [41–43]. Though other generic corrections have been proposed [44–46], for the present analysis the equation derived by Schulz [39] for ellipsoidal pores with variable orientation and shape factors has been taken $(k/k_0 = (1-P)^X$, $X = (1-\cos^2\alpha)/1 - F + \cos^2\alpha/2F$, $F =$ pore shape factor, $\alpha =$ ellipsoids orientation angle), as it has been found to better describe the different situations in the fuel [42,47].

Thus, in Fig. 11 three k/k_0 vs. P curves of the Schulz-type [39] are given, namely with the exponents $X = 1.5$, 2.5 and 3.5, which are thought to represent the first one the rim material and the other two the limits of variation of the non-rim transformed fuel. Indeed, the exponent $X = 1.5$ corresponds to a system of unordered spherical pores [39] (mimic rim). On the other hand, the exponents $X = 2.5$ and 3.5 would empirically describe, respectively, the average fuel microstructure [40,42] and specifically the influence of the lenticular grain face bubbles or pores formed during irradiation [41,42]. Very likely, data of the non-rim-transformed fuel would lie between these two lines.

The different k/k_0 curves shown in Fig. 11 would thus indicate about 20% less deterioration of the thermal conductivity of the rim material, than may be expected on the basis of the as-sintered or low-burn-up microstructures. If confirmed, this difference may imply lower calculated fuel temperatures and consequently lower gas release probability. An experimental confirmation of this possible k/k_0 vs. P trend at high burn-ups appears therefore worthwhile.

Regarding the mechanical properties, the same kind of behaviour as for the thermal conductivity may be expected for the Young's modulus, i.e. leading probably to a stiffer response of the rim material compared to the non-rim-transformed fuel at equivalent porosity

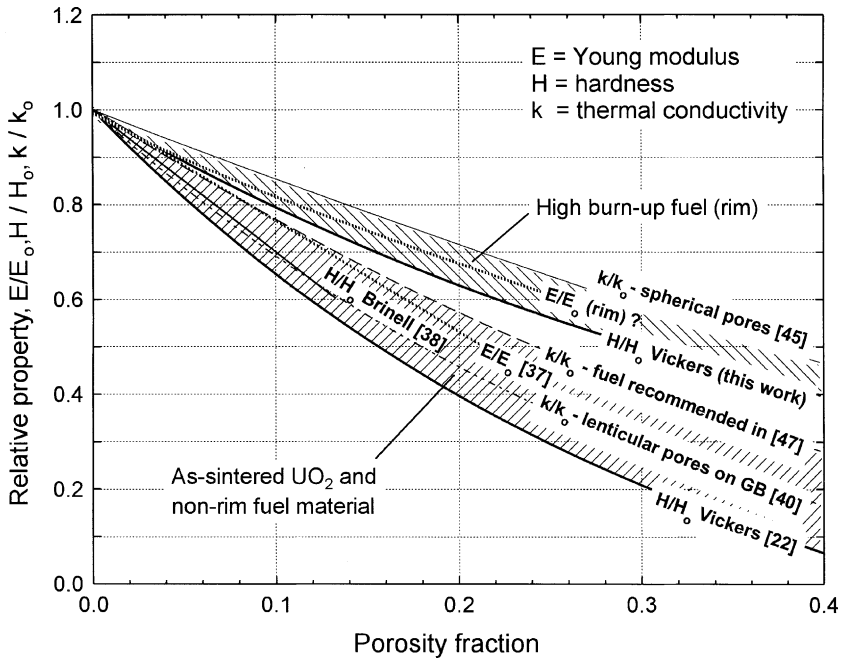

Fig. 11. Various measured and estimated 'relative property vs. porosity' relations for non-irradiated and irradiated UO_2.

(Fig. 11). In this sense, new acoustic measurements in the low burn-up fuel confirmed an E/E_0 vs. P dependence as given by randomly oriented oblate pores of axial ratio ≈0.25, i.e. sensibly below the behaviour expected for spherical pores [48]. This trend coincides at low P with the straight curve shown in Fig. 11 for sintered UO_2 [37]. Additional E-modulus measurements in high burn-up fuels (rim) as a function of porosity would be therefore worthwhile to confirm the expected stiffer behaviour of this material.

7. Summary and conclusions

The present results demonstrate first of all the utility of a rather simple experimental technique like the Vickers hardness tests in characterising high burn-up LWR fuels. It is obtained by this means not only the trend in mechanical behaviour (see also part 2), but also valuable information of microstructure features influencing other structure sensitive properties, i.e. thermal conductivity and fission gas release, including also the evolution of irradiation defects.

From the mechanistic point of view, the most important finding in this work is that *the UO_2–LWR fuels are found to become twofold softer in the course of the irradiation*. The first softening process is detected at the fuel periphery when the local burn-up exceeds ≈70 GWd/tM, essentially as a result of the porosity build-up after the rim transformation. The second softening process is found to affect uniformly the whole fuel after it reaches in average ≈70 GWd/tM, as a result of a mechanism that ostensibly denotes the bulk healing of the accumulated irradiation defects (Fig. 6).

We note that both peripheral and bulk fuel softenings are detected at a critical burn-up that coincides fairly well with that found by EPMA [49] and micro-XRD [13] for the onset of the rim-structure formation. Also worthy to note is that at higher average burn-ups than the mentioned threshold (⩾70 GWd/t M), a rim-like process is progressively observed in fuels in regions adjacent to the rim zone, with features similar to the fuel-edge process [14]. It is deduced that a rim or rim-like restructuring process can occur at any radial position in the fuel provided that the critical burn-up has been reached, and provided also that the accumulated irradiation damage has not been previously removed e.g. by thermal means, e.g. through temperatures exceeding the thermal defect-release threshold (≈1400 °C under irradiation [17]).

The other interesting result is the characterisation of the fuel hardness vs. porosity dependence, from which it can be derived that through the formation of the rim structure, *the stiffest possible pore configuration in the fuel is achieved*. As corroborated by application of the MSA model [10,20,23–27], random models [31–33] and a site-bond percolation approach model [35] (Sections 4–6), the system formed at high burn-ups is found to emulate the structure of a foam-like material, in which large amounts of porosity (>30%) can be accommodated without leading to a macroscopic pore-phase opening. As a technological spin-off of this result, *the rim material would be considered to effectively retain the fission gases occluded in pores up to relatively high local burn-ups (≈300 GWd/t M)*, since only at these burn-ups porosity fractions >0.3 may be reached, for which incipient pore interconnection might just appear.

Finally, applying the concepts of the MSA-formulation, i.e. postulating that both mechanical and thermal properties in the porous solid would follow similar porosity dependences as determined by the load bearing area [10,20,23–27], a less pronounced porosity deterioration of the Young's modulus and the thermal conductivity of the rim-zone in comparison to the fresh or low burn-up (non-rim-transformed) fuel is envisaged, as it was observed for the hardness. A technological consequence of this is that *the high burn-up fuel would run cooler in the reactor than it would be assumed from its thermal conductivity vs. porosity behaviour at low burn-ups*, leading to lower assessed fission gas release probability in the rim and neighbour zones. Specific experiments to prove this potential trend, also as a function of temperature, appear worthwhile.

References

[1] M.R. Billaux, L.F. Van Swam, S.H. Shann, in: Proceedings of the International Topical Meeting on LWR Fuel Performance, West Palm Beach, Florida, 17–21 April 1994, p. 242.
[2] F. Lemoine, M. Balourdet, in: Proceedings of the International Topical Meeting on Light Water Reactor Fuel Performance, Portland, Oregon, USA, 2–6 March 1997, p. 693.
[3] D. Vollath, in: Uranium Dioxide, UO_2, Physical Properties, Gmelin Handbook of Inorganic Chemistry, Suppl. vol. C5, Springer Verlag, 1986, p. 8.
[4] R. Manzel, M. Coquerelle, in: Proceedings of ANS International Topical Meeting on Light Water Reactor Performance, Portland, Oregon, USA, 2–6 March 1997, p. 463.
[5] B.R. Lawn, D.B. Marshall, J. Amer. Ceram. Soc. 62 (1979) 347.
[6] D. Laux, G. Despaux, D. Baron, J. Spino, in: 7th International Conference on CANDU Fuel, Kingston, Ontario, Canada, 23–27 September 2001.
[7] W.C. Oliver, G.M. Pahr, J. Mater. Res. 7 (1992) 1564.
[8] J. Spino, K. Vennix, M. Coquerelle, J. Nucl. Mater. 231 (1996) 179.
[9] Hj. Matzke, J. Spino, J. Nucl. Mater. 248 (1997) 170.
[10] R.W. Rice, Porosity of Ceramics, Marcel Dekker, 1998.
[11] J. Spino, D. Baron, M. Coquerelle, A. Stalios, J. Nucl. Mater. 256 (1998) 179.

[12] J. Cobos, D. Papaioannou, J. Spino, M. Coquerelle, J. Alloy Compd. 271–273 (1998) 610.
[13] J. Spino, D. Papaioannou, J. Nucl. Mater. 281 (2000) 146.
[14] R. Manzel, C.T. Walker, J. Nucl. Mater. 301 (2002) 170.
[15] D. Tabor, The Hardness of Metals, Clarendon, Oxford, 1951.
[16] A. Iost, R. Bigot, J. Mater. Sci. 31 (1996) 3573.
[17] W. Dienst, D. Brucklacher, in: Proceedings of the International Symposium on Ceramic Nuclear Fuels, 3–8 May 1969, Washington, The American Ceramic Society, 1969, p. 82.
[18] J. Spino, ITU Activity Report 2001, EUR 20252, 2002, p. 54.
[19] J. Spino, C.T. Walker, R. Manzel, J. Nucl. Mater., in press.
[20] R.W. Rice, C.Cm. Wu, F. Borchelt, J. Amer. Ceram. Soc. 77 (1994) 2539.
[21] A. Krell, P. Blank, J. Amer. Ceram. Soc. 78 (1995) 1118.
[22] J.L. Bates, AEC R&D Rep. HW-77799, 1963, from [3].
[23] R.W. Rice, J. Mater. Sci. 31 (1996) 1509.
[24] R.W. Rice, J. Mater. Sci. 31 (1996) 102.
[25] R.W. Rice, Key Eng. Mater. 115 (1996) 1.
[26] R.W. Rice, J. Amer. Ceram. Soc. 76 (1993) 1801.
[27] R.W. Rice, J. Mater. Sci. 32 (1997) 4731.
[28] A.K. Mukhopadhyay, K.K. Phani, J. Europ. Ceram. Soc. 20 (2000) 29.
[29] C. Reynaud, F. Thevenot, J. Mater. Sci. Lett. 19 (2000) 871.
[30] C.T. Herakovich, S.C. Baxter, J. Mater. Sci. 34 (1999) 1595.
[31] A. Roberts, E.J. Garboczi, J. Amer. Ceram. Soc. 83 (2000) 3041.
[32] S. Torquato, Appl. Mech. Rev. 44 (1991) 37.
[33] E. Garboczi, K. Snyder, J. Douglas, M. Thorpe, Phys. Rev. E: Stat. Phys. 52 (1995) 819.
[34] D. Schrire, I. Matsson, B. Grapengiesser, in: Proceedings of the ANS International Topical Meeting on LWR Performance, Portland, Oregon, USA, 2–6 March 1997, p. 104.
[35] C. Ronchi, J. Nucl. Mater. 84 (1979) 55.
[36] K. Masche, H. Overhof, P. Thomas, Phys. Stat. Sol. B 60 (1973) 563.
[37] J. Boocock, A.S. Furzer, J.R. Matthews, AERE-M 2565, 1972, from [3].
[38] P. Gondi, S. Granata, R. Tognato, Energ. Nucl. (Milan) 20 (1973) 406 (from [3]).
[39] B. Schulz, High Temp.–High Press. 13 (1981) 649.
[40] P.W. Winter, D.A. MacInnes, IAEA Technical Committee Meeting on Water Reactor Fuel Element Computer Modelling in Steady-state, Transient and Accident Conditions, Preston, England, IAEA-TC-659/5.6, 1988.
[41] J.H. Harding, D.G. Martin, P.E. Potter, Commission of the European Communities Report EUR 12402 EN, 1989.
[42] INSC-Materials Property Data Base: Thermal conductivity of solid UO_2. International Nuclear Safety Center, Argonne National Laboratory, USA. Assessed 1996, last modified Aug 25/99. Available from http://www.insc.anl.gov/matprop/uo2/kuo2s.html.
[43] D.G. Martin, J. Nucl. Mater. 110 (1982) 73.
[44] A.L. Loeb, J. Amer. Ceram. Soc. 37 (1954) 96.
[45] R. Brandt, G. Neuer, J. Non-Equilib. Thermodyn. 1 (1976) 3.
[46] J.C. Maxwell, A Treatise on Electricity and Magnetism, vol. 1, 3rd ed., Oxford University, London, 1892.
[47] K. Bakker, H. Kwast, E.H.P. Cordfunke, J. Nucl. Mater. 226 (1995) 128.
[48] J.M. Gatt, Y. Monerie, D. Laux, D. Baron, J. Nucl. Mater., in press.
[49] C.T. Walker, J. Nucl. Mater. 275 (1999) 56.